RSC Advances

PAPER

View Article Online
View Journal | View Issue

Check for updates

Cite this: *RSC Adv.*, 2023, **13**, 26015

Crystal growth, phase transition, and nuclear magnetic resonance of organic–inorganic hybrid perovskite $NH_2(CH_3)_2CdCl_3$†

Ae Ran Lim *[a,b] and Ma Byong Yoon[b]

Understanding the physicochemical properties of organic–inorganic hybrid materials is essential to promote their applications. In this study, a single crystal of $NH_2(CH_3)_2CdCl_3$ was grown, and it exhibited a monoclinic structure. Its phase transition temperatures were 460 and 470 K, and it showed sufficient thermal stability. The changes in the NMR chemical shifts of each atom in the crystal with increasing temperature were determined; the chemical shift of ^{1}H of NH_2 in the $NH_2(CH_3)_2$ cation changed with temperature, which was correlated to the changes in the chemical shift of ^{14}N in NH_2. The change in ^{113}Cd chemical shifts indicate the change of six Cl atoms around Cd in $CdCl_6$. Therefore, the change in the coordination geometry of $CdCl_6$ is attributed to the change in the N–H⋯Cl hydrogen bond between the $NH_2(CH_3)_2$ cation and $CdCl_6$ anion. In addition, the ^{13}C activation energies E_a obtained from the spin-lattice relaxation time $T_{1\rho}$ values are smaller than those of the ^{1}H E_a values, suggesting that is free compared to ^{1}H in the cation. We believe that this study furthers our fundamental understanding of organic–inorganic hybrid materials to promote their practical solar cell applications.

Received 30th June 2023
Accepted 21st August 2023

DOI: 10.1039/d3ra04381a

rsc.li/rsc-advances

1. Introduction

Organic–inorganic hybrid perovskite crystals based on metal halides have received increasing attention owing to their interesting optoelectronic, electrical, and magnetic properties.[1–5] The most common perovskite $MAPbX_3$ (MA = CH_3NH_3, X = I, Br, or Cl) based thin-film photovoltaic devices are used as solar cells.[6–14] However, $MAPbX_3$-based photovoltaics are highly unstable under ambient conditions, especially in the presence of moisture, and are highly toxic owing to Pb bioaccumulation. Recently, researchers have suggested substituting Pb with other low-toxicity or eco-friendly metals to develop Pb-free photovoltaic devices. Free-Pb $[NH_3(CH_2)_nNH_3]BX_4$ (n = 1, 2, 3…, B = Mn, Co, Cu, Zn, or Cd) and $[C_nH_{2n+1}NH_3]_2BX_4$ are organic–inorganic hybrids that have recently attracted considerable attention.[15–27] In addition, $[NH_2(CH_3)_2]_2BX_4$ and $NH_2(CH_3)_2BX_3$ are MA_2BX_4- and $MABX_3$-type complexes, where MA^+ (= $NH_2(CH_3)_2$) is a univalent cation.[28–34] Here, the organic group of the organic–inorganic hybrid material determines the optical properties and structural flexibility of the material, whereas the inorganic group affects the mechanical and thermal properties. Hence, these organic–inorganic materials constitute an important area of research in the field of materials science.[35,36]

X-ray studies on dimethylammonium trichlorocadmium crystals, $NH_2(CH_3)_2CdCl_3$, revealed their monoclinic structure with a $P2_1/c$ space group and the lattice parameters a = 8.7377 Å, b = 13.2709 Å, c = 6.6910 Å, β = 98.371°, and Z = 4 at room temperature.[37] The structural unit is formed by the organic $[NH_2(CH_3)_2]^+$ and the inorganic $[CdCl_6]^-$ moieties. The infinite chains consist of face-sharing $CdCl_6$ octahedra, resulting in a 1D perovskite structure of the $MABX_3$ family, where MA = $NH_2(CH_3)_2$, B = Cd, and X = Cl. The six doubly bridging chloride ions link the adjacent Cd centers *via* Cd–Cl bonds.

Moreover, Kalthoum *et al.*[37] investigated the application of $NH_2(CH_3)_2CdCl_3$, which has a large dielectric constant, in field-effect transistors. They also reported the optical properties of $NH_2(CH_3)_2CdCl_3$ for solar cell applications.[38] And, the effects for Zn^{2+} and Cu^{2+} doping of $NH_2(CH_3)_2CdCl_3$ for white-light emission and green solar cell applications were investigated by Jellai *et al.*[39]

The minimum of nuclear magnetic resonance (NMR) spin-lattice relaxation time in the rotating frame ($T_{1\rho}$) depends on the frequency ω_1 rather than ω_o. Therefore, the minimum $T_{1\rho}$ is observed at a lower temperature than the spin–lattice relaxation time in the laboratory frame (T_1). $T_{1\rho}$ provides information on motion in the kHz region, and T_1 provides information on rapid motion in the order of tens or hundreds of MHz.[40]

---

[a] *Graduate School of Carbon Convergence Engineering, Jeonju University, Jeonju 55069, Korea*

[b] *Department of Science Education, Jeonju University, Jeonju 55069, Korea. E-mail: aeranlim@hanmail.net; arlim@jj.ac.kr*

† Electronic supplementary information (ESI) available. CCDC The datasets generated and/or analysed during the current study are available in the CCDC 2258449. For ESI and crystallographic data in CIF or other electronic format see DOI: **https://doi.org/10.1039/d3ra04381a**

In this study, among the perovskite types applied to solar cell applications, single crystals of Pb-free and thermal stable materials are grown and their physicochemical properties are studied. Therefore, we grew a $NH_2(CH_3)_2CdCl_3$ single crystal *via* an aqueous solution method and analyzed its structure by single-crystal X-ray diffraction (SCXRD). The phase transition temperature (T_C) of this crystal was determined using differential scanning calorimetry (DSC) and powder X-ray diffraction (PXRD). Thermogravimetric analysis (TGA) was performed to determine the thermodynamic properties of the material. The structural environments of ^1H, ^{13}C, ^{14}N, and ^{113}Cd in $[NH_2(CH_3)_2]$ cation and $CdCl_6$ anion were analyzed based on the chemical shifts observed in magic angle spinning (MAS) NMR and static NMR spectra. Moreover, we determined the $T_{1\rho}$, which represents the energy transfer around the ^1H and ^{13}C atoms of the cation, and activation energies (E_a). These physicochemical properties can provide important insights into the mechanisms of compound for potential applications in solar cell.

2. Experimental

2.1. Crystal growth

$NH_2(CH_3)_2CdCl_3$ single crystals were grown from a mixture of a 1 : 1 ratio of $NH_2(CH_3)_2Cl$ (99%; Sigma-Aldrich) and $CdCl_2$ (99.99%; Sigma-Aldrich) in an aqueous solution. The mixture was heated and stirred to form a saturated solution. After filtering the prepared solution through a filter, the colorless and transparent single crystals were grown for a few weeks *via* slow evaporation at a constant temperature of 300 K.

2.2. Characterization

Lattice constants were obtained at 200 K and 300 K using the SCXRD instrument at the Seoul Western Center of the Korea Basic Science Institute (KBSI). A single crystal in Paratone oil was placed on a Bruker diffractometer (D8 Venture PHOTON III M14) equipped with a graphite-monochromated Mo-Kα radiation source ($\lambda = 0.71073$ Å) and a N_2 cold flow (−50 °C). The data were collected and integrated using SMART APEX3 (Bruker, 2016) and SAINT (Bruker, 2016). The absorption was corrected using the multiscan method implemented in SADABS. This structure was analyzed by full-matrix least-squares on F^2 using the SHELXTL software.[41] All hydrogen atoms are represented by geometric positions. In addition, the PXRD patterns of the $NH_2(CH_3)_2CdCl_3$ were obtained at various temperatures with a Mo-Kα target.[42]

DSC measurements (DSC 25, USA) were acquired in the range of 200–573 K at a heating rate of 5 °C min^{-1} and 10 °C min^{-1} under N_2 gas, respectively.

TGA (SDT 0650-0439, USA) and differential thermal analysis (DTA) were performed in the range of 300–873 K at a heating rate of 10 °C min^{-1} under N_2 gas.

The ^1H MAS and ^{13}C cross-polarization (CP) MAS NMR spectra of $NH_2(CH_3)_2CdCl_3$ crystals were recorded at the Larmor frequencies of 400.13 and 100.61 MHz using a solid-state 400 MHz NMR spectrometer (AVANCE III+, Bruker, Germany) at the KBSI Seoul Western Center. The samples in the cylindrical zirconia rotors were spun at a rate of 10 kHz for the MAS NMR measurements to minimize the spinning sideband. Adamantane and tetramethylsilane (TMS) were selected as the internal standards for ^1H and ^{13}C NMR, respectively. 1D NMR spectrum for ^1H and ^{13}C was performed in the delay time of 1.5–15 s. The ^1H $T_{1\rho}$ values were measured using $\pi/2$–τ spin-lock pulse for a duration of τ, and the $\pi/2$ pulse width was 4 μs. And, the ^{13}C $T_{1\rho}$ values were measured by varying the duration of a ^{13}C spin-locking pulse applied after the CP preparation period. The ^{13}C $T_{1\rho}$ values were obtained using CP-τ acquisition. Static ^{14}N NMR spectra of the $NH_2(CH_3)_2CdCl_3$ crystal were recorded using the one-pulse method with a Larmor frequency of 28.90 MHz, where NH_4NO_3 was the internal standard. Static ^{113}Cd NMR spectra were recorded at a Larmor frequency of 88.75 MHz, where $CdCl_2O_8 \cdot 6H_2O$ was the internal standard. The NMR experiment above 430 K due to the limitations of the NMR instrument was not possible. The temperature was maintained nearly constant within the error range of ±0.5 °C, even when the rate of N_2 gas flow and the heater current were adjusted.

3. Results and discussion

3.1. Single crystal XRD

The SCXRD results at 200 K and 300 K showed that $NH_2(CH_3)_2CdCl_3$ crystallized into a monoclinic system with a $P2_1/c$ space group. The cell constants were as follows: $a = 8.6891$ (13) Å, $b = 13.212$ (2) Å, $c = 6.6851$ (10) Å, $\beta = 98.362°$ (2), and $Z = 4$. Fig. 1 shows the structure of the $NH_2(CH_3)_2CdCl_3$ crystal at 200 K, and the SCXRD data at 200 K and 300 K are presented in Table 1. The structure constitutes an organic $[NH_2(CH_3)_2]^+$ cation and inorganic $[CdCl_6]^-$ anion. The infinite chains consisted of face-shared $CdCl_6$ octahedra and six doubly bridging Cl^- ions linked to adjacent Cd centers. The bond lengths and angles are summarized in Table 2. Moreover, N–H···Cl

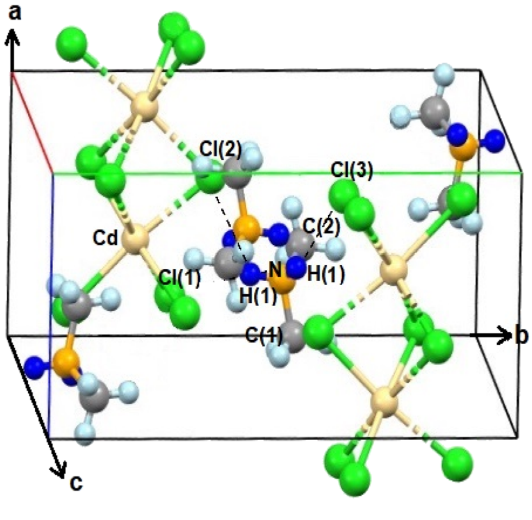

Fig. 1 Crystal structure of $NH_2(CH_3)_2CdCl_3$ at 200 K (A.R. Lim CCDC 2258449).

Table 1 Crystal data and structure refinement for $NH_2(CH_3)_2CdCl_3$ at 200 K and 300 K. The full data available in the CIF files

Chemical formula	$C_2H_8NCdCl_3$	$C_2H_8NCdCl_3$
Weight	264.84	264.84
Crystal system	Monoclinic	Monoclinic
Space group	$P2_1/c$	$P2_1/c$
T (K)	200	300
a (Å)	8.6891 (13)	8.7426 (5)
b (Å)	13.212 (2)	13.2834 (8)
c (Å)	6.6851 (10)	6.6950 (3)
β (°)	98.362 (2)	98.362 (2)
Z	4	4
V (Å^3)	759.0 (2)	769.23 (7)
Radiation type	Mo-Kα	Mo-Kα
Wavelength (Å)	0.71073	0.71073
Reflections collected	14 048	13 392
Independent reflections	1871 (R_{int} = 0.0582)	1932 (R_{int} = 0.0925)
Goodness-of-fit on F^2	1.078	1.079
Final R indices [I > 2sigma(I)]	wR_1 = 0.0234, wR_2 = 0.0615	wR_1 = 0.0884, wR_2 = 0.2946
R indices (all data)	wR_1 = 0.0244, wR_2 = 0.0621	wR_1 = 0.0936, wR_2 = 0.3043

Table 2 Bond-lengths (Å) and bond-angles (°) for $NH_2(CH_3)_2CdCl_3$ at 200 K and 300 K

Temperature	200 K	300 K
Cd–Cl(1)	2.6062 (6)	2.5927 (18)
Cd–Cl(2)	2.5872 (6)	2.6076 (19)
Cd–Cl(3)	2.6613 (6)	2.659 (2)
Cd–Cl(1)#2	2.6788 (6)	2.6803 (18)
Cd–Cl(2)#1	2.6223 (6)	2.6226 (19)
Cd–Cl(3)#1	2.6860 (6)	2.6933 (19)
N(1)–C(1)	1.472 (4)	1.456 (12)
N(1)–C(2)	1.479 (3)	1.463 (13)
N(1)–H(1AN)	0.9100	0.8900
N(1)–H(1BN)	0.9100	0.8900
C(1)–H(1)	0.9800	0.9600
C(2)–H(2)	0.9800	0.9600
Cl(2)–Cd–Cl(1)	99.17 (2)	98.83 (6)
Cl(2)–Cd–Cl(3)	84.59 (2)	84.67 (6)
Cl(1)–Cd–Cl(3)	176.126 (18)	176.38 (6)
H(1AN)–Cl(2)	2.792	2.697
H(1BN)–Cl(3)	2.551	2.590
N(1)–H(1AN)–Cl(2)	122.09	141.02
N(1)–H(1BN)–Cl(3)	148.93	150.24

hydrogen bonds connected the $[NH_2(CH_3)_2]^+$ cations to the $[CdCl_6]^-$ anions. Here, the N–H⋯Cl hydrogen bond consists of an angle greater than 120° as shown in Table 2.[43]

3.2. Phase transition temperatures and thermal properties

DSC results were obtained in the temperature range of 200–573 K at a heating rate of 5 and 10 °C min^{-1} by putting powder sample of 15.2 mg and 5.7 mg in a capsule, respectively. Two weak endothermic peaks at 461 and 470 K and one strong endothermic peak at 549 K were shown in Fig. 2. The enthalpies for the three observed peaks in the heating rate of 10 °C min^{-1} were 20.44, 73.16, and 690.68 kJ mol^{-1}.

In addition, TGA experiment with the amount of 8.35 mg was conducted at a heating rate of 10 °C min^{-1} the same as the DSC experiment, and the results are shown in Fig. 2 in detail. The crystal was thermally stable up to 524 K with a weight loss of ∼2%. The endothermic peak at ∼547 K confirms the peak observed in the DSC curve. Moreover, the fact that the crystal became opaque at ∼550 K suggests that ∼550 K is the decomposition temperature (T_d) of the crystal. From the total molecular weight of 264.86 mg, the amounts of residual produced by the decomposition of HCl and $[NH_2(CH_3)_2Cl]$ were considered. The molecular weight losses of 14 and 31% were due to the decomposition of HCl and $[NH_2(CH_3)_2Cl]$, respectively. As the two step decomposition processes, the first undergo a weight loss of 14% near 573 K, and the second undergo a weight loss of 31% near 784 K.

In order to accurately confirm the three peaks shown in the DSC results of Fig. 2, we observed the changes in the single crystal with temperature using an optical polarization microscope. No significant changes were observed when the temperature was increased from 300 to 500 K, following which

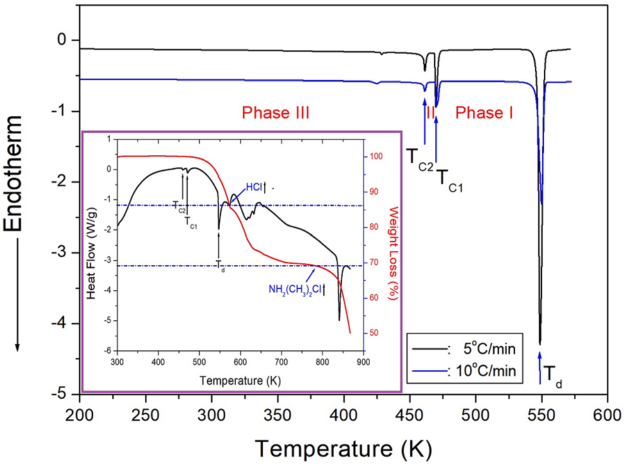

Fig. 2 Differential scanning calorimetry curves of $NH_2(CH_3)_2CdCl_3$ measured with the heating rates of 5 and 10 °C min^{-1} (inset: thermogravimetry and differential thermal analysis curves of $NH_2(CH_3)_2CdCl_3$).

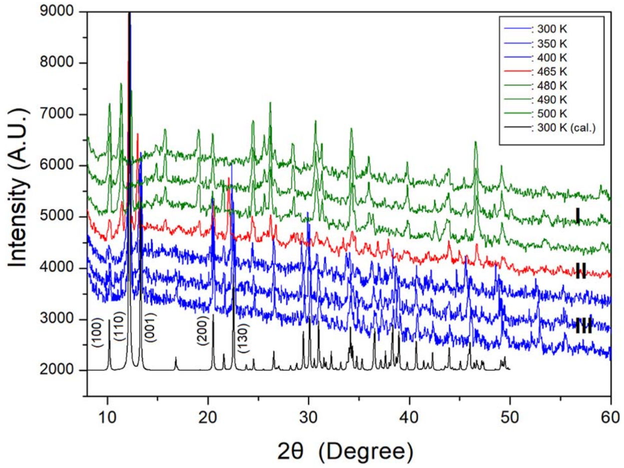

Fig. 3 Powder X-ray diffraction patterns of $NH_2(CH_3)_2CdCl_3$ at phases III, II, and I. 300 K (cal.) is the theoretical XRD pattern at 300 K.

the crystal gradually became opaque at higher temperatures. The single crystal became completely opaque at ~550 K and melted at 600 K.

PXRD patterns were acquired at different temperatures in the 2θ range of 8–60° as shown in Fig. 3. The PXRD patterns obtained at 300, 350, and 400 K (blue color) of phase III differ slightly from that recorded at 465 K (red color) of phase II; this difference is associated with T_{C2} (= 461 K). Furthermore, the PXRD pattern recorded at 465 K of phase II differs from those recorded above 480 K (olive color) of phase I, indicating a clear change in T_{C1} (= 470 K). These results are consistent with those of the DSC experiments. Additional, the theoretical XRD pattern based on the cif file at 300 K is shown in Fig. 3, which agrees well with the experimental pattern. The peaks observed in this diffractogram are indexed with Mercury program.

Therefore, the DSC, PXRD, and polarizing microscopy experiments suggest that the phase transition temperatures were $T_{C2} = 461$ K and $T_{C1} = 470$ K, whereas the decomposition temperature was $T_d = 549$ K.

3.3. ^1H and ^{13}C MAS NMR chemical shifts

Two ^1H NMR spectra by NH_2 and CH_3 in $NH_2(CH_3)_2CdCl_3$ should be obtained, but only one signal was obtained, and these results are shown in Fig. 4(a). At low temperatures, the two ^1H NMR signals completely overlapped. The sideband of the ^1H NMR spectrum is marked by *. As the temperature increased, they separated slightly.

One sideband appears on the right side and two sidebands appear on the left side. The appearance of two sidebands (oval on the left side) indicated that the two ^1H signals in NH_2 and CH_3 did not completely overlap. That is, at 430 K, the ^1H chemical shift in CH_3 was 3.24 ppm and the ^1H chemical shift in NH_2 was ~5 ppm as shown in Fig. 4(b). Here, the sidebands for NH_2 and CH_3 are marked by open circles and crosses, respectively; moreover, the half widths (A and B) of full width at half maximum (FWHM) at 180, 300, and 400 K were not symmetrical (inset of Fig. 4(b)). The ^1H peak of CH_3 hardly changed with temperature, suggesting that the structural environment around ^1H in CH_3 does not change with temperature. However, the fact that the sideband on the left side appears as one at low temperatures and two at high temperatures indicates that the position of the ^1H signal in NH_2 changes slightly with temperature. This result indicates that the environments around ^1H in NH_2 vary slightly with the temperature.

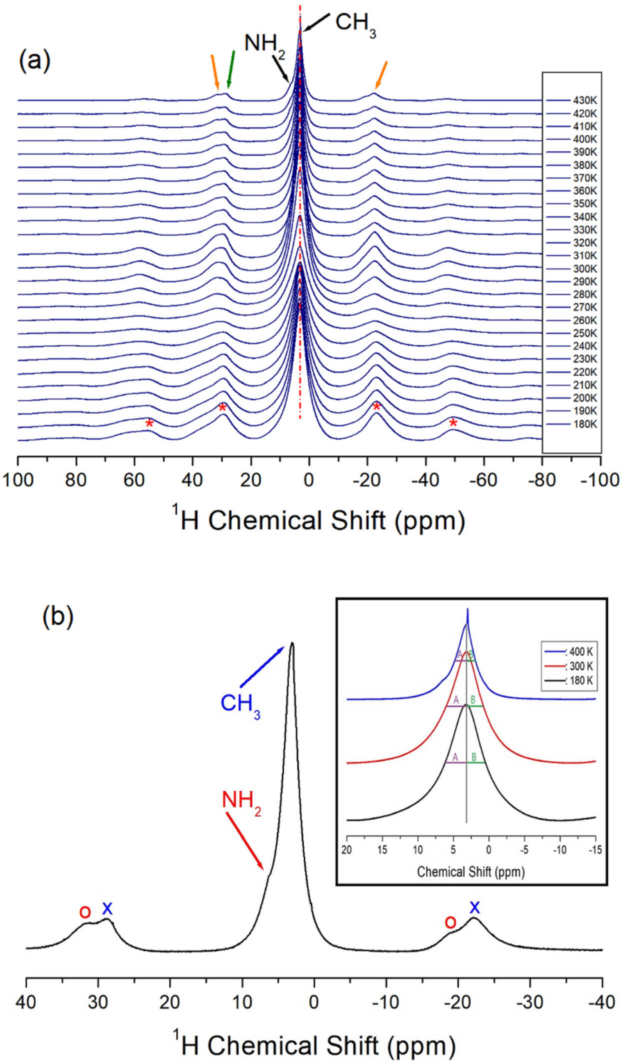

Fig. 4 (a) ^1H MAS NMR chemical shifts for $NH_2(CH_3)_2CdCl_3$ as a function of temperatures. Asterisks are sidebands for ^1H NMR signal (inset: halfwidths A and B of full width at half maximum at 180, 300, and 400 K), and (b) ^1H MAS NMR chemical shift for NH_2 and CH_3 at 430 K.

The ^{13}C MAS NMR chemical shifts of $NH_2(CH_3)_2CdCl_3$ were measured at increasing temperatures, as shown in Fig. 5. Two signals for ^{13}C were recorded at 220 K, indicating that the two ^{13}C atoms of the cation had different environments. At 260 K, only one signal is observed, indicating that the environment surrounding ^{13}C remains the same. However, at 300 K and 340 K, two separate ^{13}C spectra were observed, indicating that the surrounding environments of ^{13}C in the cation were different from each other. In other words, the observation of the two ^{13}C NMR signals means that the surrounding environments of the two CH_3 located on both sides of N in the $NH_2(CH_3)_2$ cation are different each other. And, the observation of one ^{13}C NMR

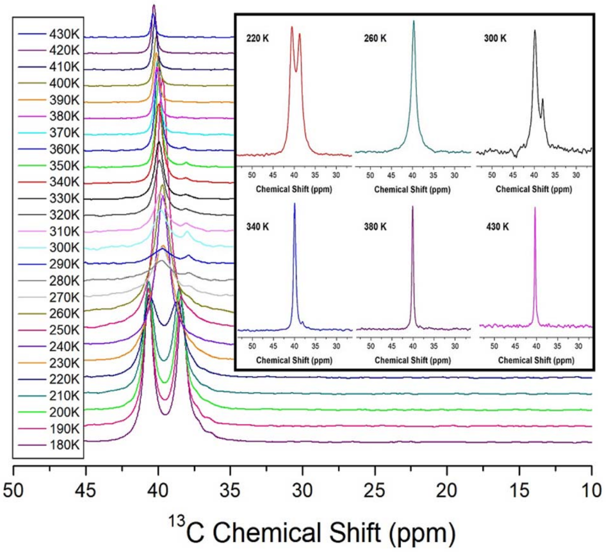

Fig. 5 ^{13}C MAS NMR chemical shifts for $NH_2(CH_3)_2CdCl_3$ as a function of temperature (inset: ^{13}C MAS NMR chemical shifts for $NH_2(CH_3)_2CdCl_3$ at 220, 260, 300, 340, 380, and 430 K).

signal means that the surrounding environments of the two CH_3 located on both sides of N are the same each other. Finally, at temperatures above 380 K, a single spectrum was observed, and the line width became very narrow. Hence, the environments around ^{13}C in CH_3 vary considerably depending on the temperature. ^{13}C NMR chemical shifts were observed at 39.84 and 37.97 ppm at 300 K, and the line width was narrower (1.54 ppm) than that (32 ppm) in the ^{1}H NMR of NH_2 and CH_3, indicating that the molecular motion of ^{13}C located at the end of the $[NH_2(CH_3)_2]$ cation is very free.

3.4. ^{14}N and ^{113}Cd static NMR chemical shift

The ^{14}N static NMR spectrum of NH_2 in the $NH_2(CH_3)_2CdCl_3$ single crystal was recorded in the temperature range of 180–420 K as shown in Fig. 6. The ^{14}N NMR spectrum was less sensitive than ^{1}H, but has a larger chemical shift range. The magnetic field direction relative to the single-crystal direction was measured in an arbitrary direction. The NMR spectrum due to the spin number of ^{14}N ($I = 1$)[44] was predicted by the two resonance lines owing to the quadrupole interaction. The Larmor frequency for ^{14}N NMR spectrum was extremely low as 28.90 MHz, which made it difficult to obtain a signal. Moreover, distinguishing the signals was difficult owing to the low peak intensities and wide line widths. Four ^{14}N NMR signals were observed, which were divided into two sets: N(1) and N(2). The chemical shift of N(1) slightly increased with increasing temperature, whereas that of N(2) decreased and then slightly increased. At 300 K, the line width was extremely broad (∼64 ppm) and indicated the presence of two sets of N sites. The continuous changes in the N(1) and N(2) chemical shifts with increasing temperature indicated a change in the coordination geometry of the local environment of ^{14}N atom. SCXRD results did not indicate different N sites; thus, these two sets of ^{14}N NMR signals suggest a twin structure due to the property of ferroelastic materials.

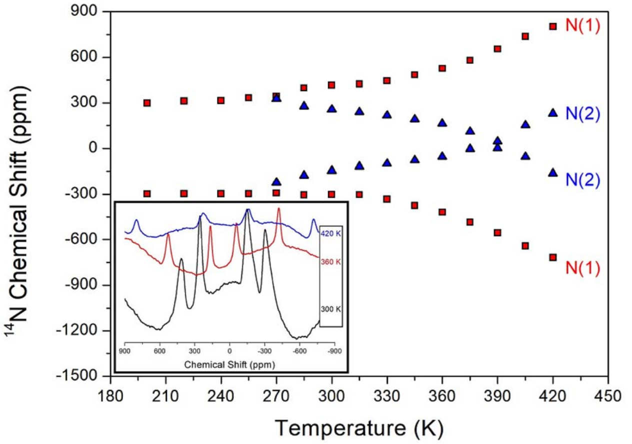

Fig. 6 The static ^{14}N NMR chemical shifts of $NH_2(CH_3)_2CdCl_3$ single crystal as a function of temperature (inset: ^{14}N NMR spectrum at 300, 360, and 420 K).

The ^{113}Cd signal was distributed over a wide chemical shift range and exhibited good intensity owing to its relatively high natural abundance; therefore, it was not difficult to record. From the chemical shifts of static ^{113}Cd NMR, the structural environment around ^{113}Cd in $CdCl_6$ was determined based on the temperature change. As the number of spins in ^{113}Cd ($I = \frac{1}{2}$),[44] only one resonance signal was expected. At 300 K, the ^{113}Cd chemical shift was 215.26 ppm as shown in Fig. 7, and the ^{113}Cd chemical shifts changed with temperature, suggesting that the ^{113}Cd environment in $CdCl_6$ changed with temperature. The line widths of the ^{113}Cd NMR spectra are shown in detail in Fig. 7. At 300 K, the line width was ∼39 ppm, which is wider than ^{1}H line widths, and hardly changed within the error range depending on the temperature.

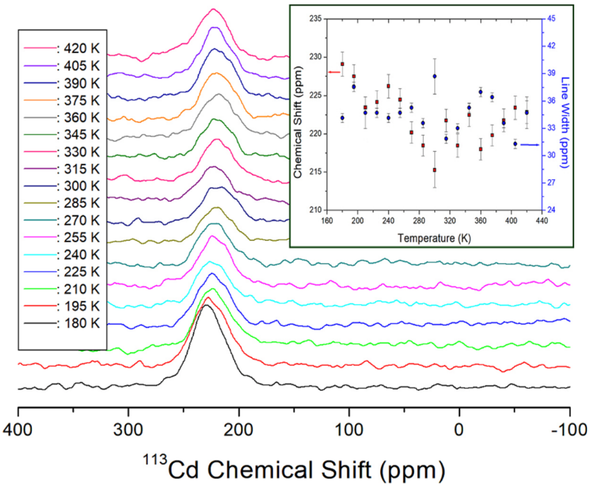

Fig. 7 Static ^{113}Cd NMR chemical shifts for $NH_2(CH_3)_2CdCl_3$ as a function of temperature (inset: ^{113}Cd NMR chemical shifts and line widths for $NH_2(CH_3)_2CdCl_3$ as a function of temperature).

3.5. ^{1}H and ^{13}C NMR spin-lattice relaxation times

The ^{1}H and ^{13}C $T_{1\rho}$ values of $NH_2(CH_3)_2CdCl_3$ crystals were collected using a spin-lock pulse and subsequent FID. The intensity changes in the measured magnetization are calculated using the following equation:[45,46]

$$S(t)/S(0) = \exp(-t/T_{1\rho}) \tag{1}$$

where $S(t)$ is the intensity of the resonance line at delay time t and $S(0)$ is the intensity of the resonance line at delay time $t = 0$. The experiment was repeated several times with different t values, and the $T_{1\rho}$ values were obtained from the slopes of the resulting intensities *vs.* the t values in eqn (1). The $T_{1\rho}$ values for ^{1}H and ^{13}C NMR of $NH_2(CH_3)_2CdCl_3$ as a function of 1000/temperature are shown in Fig. 8 and 9, respectively. The ^{1}H NMR $T_{1\rho}$ values increased slightly with increasing temperature but decreased rapidly at temperatures above 220 K with increasing temperature and subsequently increased rapidly. The minimum ^{1}H $T_{1\rho}$ value of 0.9 ms was exhibited at 300 K, and the pattern of ^{1}H $T_{1\rho}$ values shown in Fig. 8 suggests that molecular motion fits the Bloembergen–Purcell–Pound (BPP) theory. The experimental $T_{1\rho}$ value is related to the correlation time, τ_C, according to BPP theory, and the $T_{1\rho}$ value for molecular motion is expressed by eqn (2) as shown below:[40]

$$\begin{aligned}(T_{1\rho})^{-1} &= R[4J_1(\omega_1) + J_2(\omega_C - \omega_H) + 3J_3(\omega_C) + 6J_4(\omega_C + \omega_H) + 6J_5(\omega_H)]\\ J_1 &= \tau_C/\left[1 + \omega_1^{2}\tau_C^{2}\right],\ J_2 = \tau_C\Big/\left[1 + (\omega_C - \omega_H)^{2}\tau_C^{2}\right],\ J_3 = \tau_C/\left[1 + \omega_C^{2}\tau_C^{2}\right]\\ J_4 &= \tau_C\Big/\left[1 + (\omega_C + \omega_H)^{2}\tau_C^{2}\right],\ J_5 = \tau_C/\left[1 + \omega_H^{2}\tau_C^{2}\right]\end{aligned} \tag{2}$$

where $R\ (= \mu_0\hbar\gamma_H\gamma_C/\pi r^3)^2$ is a constant; ω_1 is the spin-lock field; and ω_H and ω_C are the Larmor frequencies for proton and carbon, respectively. The minimum $T_{1\rho}$ value is satisfied when $\omega_1\tau_C = 1$, and the constant R value ($= 350 \times 10^5$ for ^{1}H; 133×10^5 and 48×10^5 for ^{13}C) can be calculated by using the τ_C obtained from $\omega_1\tau_C = 1$. Using R and ω_1 values as well as the ω_H, ω_C, and $T_{1\rho}$ values obtained from the experiment, we calculated τ_C values of molecular motion as a function of temperature. The local field fluctuation is described by the thermal motion of the protons, which is caused by thermal energy. The correlation time τ_C is represented by the Arrhenius dependence of the activation energy as shown below:[45]

$$\tau_C = \tau_C(0)\exp(-E_a/k_BT) \tag{3}$$

where $\tau_C(0)$, E_a, k_B, and T are the pre-correlation time, activation energy, Boltzmann constant, and temperature, respectively. The magnitude of E_a depends on molecular dynamics. The plot of τ_C on a logarithmic scale *vs.* 1000/T for ^{1}H is shown in Fig. 8. τ_C was determined to be 44.84 ± 2.26 kJ mol^{-1} from the slope of the blue dotted line.

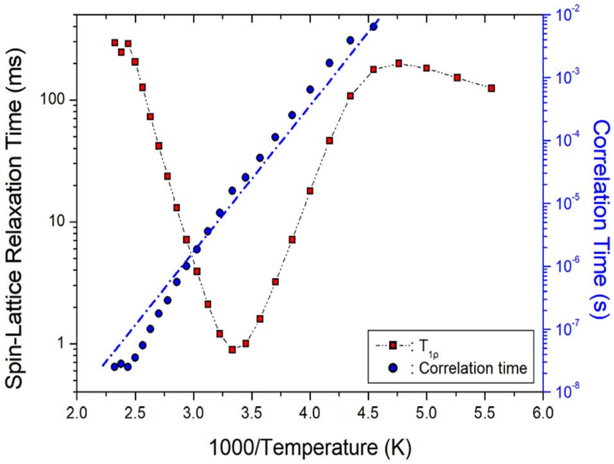

Fig. 8 ^{1}H $T_{1\rho}$ values and correlation times of $NH_2(CH_3)_2CdCl_3$ as a function of inverse temperature. Blue dot line is represented the activation energy E_a.

On the other hand, the two ^{13}C $T_{1\rho}$ values shown in Fig. 9 showed similar trends at all temperatures, and the minimum $T_{1\rho}$ value of CH_3 was observed at 280 K. The minimum ^{13}C $T_{1\rho}$ values of 6.54 and 2.32 ms were observed at 280 K. The ^{13}C $T_{1\rho}$ values varied considerably with temperature. These values first gradually increased with increasing temperature up to 220 K, above which they decreased rapidly to a minimum and finally rapidly increased. Similar to the ^{1}H $T_{1\rho}$ values, the ^{13}C $T_{1\rho}$ values exhibit molecular motion according to the BPP theory. The ^{13}C

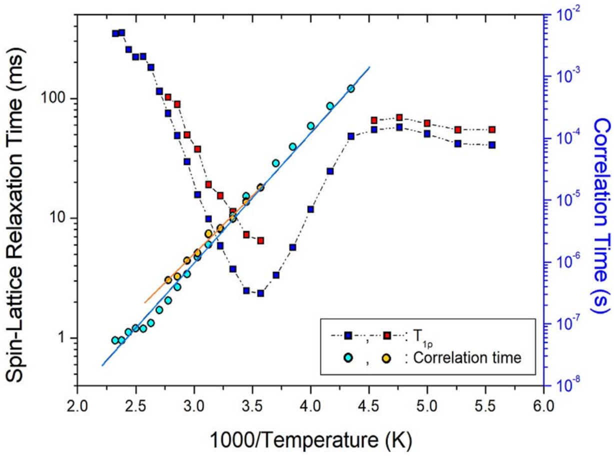

Fig. 9 ^{13}C $T_{1\rho}$ values and correlation times of $NH_2(CH_3)_2CdCl_3$ as a function of inverse temperature. Two solid lines are represented the activation energies E_a.

τ_C values were calculated using the same method as that used for the ^1H τ_C value based on the temperature change, as shown in Fig. 9. The ^{13}C E_a values obtained from the plots of τ_C *vs.* $1000/T$ were 40.77 ± 2.82 and 37.19 ± 1.91 kJ mol^{-1}; these two values are similar within the error range.

4. Conclusions

In this study, an organic–inorganic hybrid $NH_2(CH_3)_2CdCl_3$ crystal was grown and its crystal structure, phase transition temperature, thermal behavior, and structural dynamics were investigated. The structure of this crystal was monoclinic, as evidenced by SCXRD at 200 K and 300 K, and the phase transition temperatures T_C of 460 and 470 K were determined using DSC and PXRD. The thermal properties determined by TGA showed that the crystal began decomposing at 540 K and was thermally stable. Although the surrounding environments by the ^1H, ^{13}C, ^{14}N, and ^{113}Cd NMR chemical shifts varied with increasing temperature, this is independent of the phase transition. It is noteworthy that the ^1H and ^{14}N NMR chemical shifts bonded to NH_2 in the $NH_2(CH_3)_2$ cation were changed more as the temperature changes, and the change in ^{113}Cd NMR chemical shift indicate changes in the surrounding environment of the six Cl atoms around the Cd in $CdCl_6$. These experimental results suggest that the N–H⋯Cl hydrogen bonding between the $NH_2(CH_3)_2$ cation and $CdCl_6$ anion changed with temperature. In addition, $T_{1\rho}$ values which represent the energy transfer around the ^1H and ^{13}C atoms of the cation, varied significantly with temperature. ^1H and ^{13}C $T_{1\rho}$ values were comparable in the measured temperature range because ^1H and ^{13}C connect the same bond in the cation. Moreover, ^{13}C E_a values were smaller than those of ^1H, suggesting that ^{13}C at the end of the cation is free compared to ^1H in the cation. The physicochemical properties will help a fundamental understanding of Pb-free organic–inorganic perovskite type solar cell.

Conflicts of interest

There are no conflicts to declare.

Acknowledgements

This work was supported by the national Research Foundation of Korea (NRF) grant funded by the Korea government (MSIT) (2023R1A2C2006333). This research was also supported by the Basic Science Research Program through the National Research Foundation of Korea (NRF), funded by the Ministry of Education, Science, and Technology (2016R1A6A1A03012069).

References

1 R. Jlassi, A. P. C. Ribeiro, M. Mendes, W. Rekik, G. A. O. Tiago, K. T. Mahmudov, H. Naili, M. F. C. Guedes da Silva and A. J. L. Pombeiro, *Polyhedron*, 2017, **129**, 182.

2 S. Dgachi, A. M. Ben Salah, M. M. Turnbull, T. Bataille and H. Naili, *J. Alloys Compd.*, 2017, **726**, 315.

3 O. Kammoun, H. Naili, W. Rekik and T. Bataille, *Inorg. Chim. Acta*, 2015, **434**, 209.

4 S. F. Hoefler, G. Trimmel and T. Rath, *Monatsh. Chem.*, 2017, **148**, 795.

5 S.-S. Rong, M. B. Faheem and Y.-B. Li, *J. Electron. Sci. Technol.*, 2021, **19**, 100081.

6 M. Zhang, Z. Li, X. Xin, J. Zhang, Y. Feng and H. Lv, *ACS Catal.*, 2020, **10**, 14793.

7 Y. Zhu, Y. Liu, Q. Ai, G. Gao, L. Yuan, Q. Fang, X. Tian, X. Zhang, E. Egap, P. M. Ajayan and J. Lou, *ACS Mater.*, 2022, **4**, 464.

8 Q. Chen, N. D. Marco, Y. Yang, T.-B. Song, C.-C. Chen, H. Zhao, Z. Hong, H. Zhou and Y. Yang, *Nano Today*, 2015, **10**, 355.

9 M. Hermes, S. A. Bretschneider, V. W. Bergmann, D. Klasen, J. Mars, W. Tremel, F. Laquai, H.-J. Butt, M. Mezger, R. Berger, B. J. Rodriguez and S. A. L. Weber, *J. Phys. Chem.*, 2016, **120**, 5724.

10 E. Strelcov, Q. Dong, T. Li, J. Chae, Y. Shao, Y. Deng, A. Gruverman, J. Huang and A. Centrone, *Sci. Adv.*, 2017, **3**, e1602165.

11 S. K. Abdel-Aal, A. S. Abdel-Rahman, G. G. KocherOberlehner, A. Ionov and R. Mozhchil, *Acta Crystallogr. A*, 2017, **70**, C1116.

12 Y. Liu, L. Collins, R. Proksch, S. Kim, B. R. Watson, B. Doughty, T. R. Calhoun, M. Ahmadi, A. V. Ievlev, S. Jesse, S. T. Retterer, A. Belianinov, K. Xiao, J. Huang, B. G. Sumpter, S. V. Kalinin, B. Hu and O. S. Ovchinnikova, *Nat. Mater.*, 2018, **17**, 1013.

13 C. M. Mauck, A. France-lanord, A. C. Hernandez Oendra, N. S. Dahod, J. C. Grossman and W. A. Tisdale, *J. Phys. Chem. C*, 2019, **123**, 27904.

14 C. J. Dahlman, R. M. Kennard, P. Paluch, N. R. Venkatesan, M. L. Chabinyc and G. N. Manjunatha Reddy, *Chem. Matter.*, 2021, **33**, 642.

15 C. N. R. Rao, A. K. Cheetham and A. Thirumurugan, *J. Phys. Condens. Matter*, 2008, **20**, 83202.

16 Z. Cheng and J. Lin, *CrystEngComm*, 2010, **12**, 2646.

17 M. F. Mostafa and S. S. El-khiyami, *J. Solid State Chem.*, 2014, **209**, 82.

18 S. Gonzalez-Carrero, R. E. Galian and J. Perez-Prieto, *Part. Part. Syst. Char.*, 2015, **32**, 709.

19 S. K. Abdel-Adal, G. Kocher-Oberlehner, A. Ionov and R. N. Mozhchil, *Appl. Phys. A*, 2017, **123**, 531.

20 W. Liu, J. Xing, J. Zhao, X. Wen, K. Wang, P. Lu and Q. Xiong, *Adv. Opt. Mater.*, 2017, **5**, 1601045.

21 P. Mondal, S. K. Abdel-Aal, D. Das and S. K. Manirul Islam, *Catal. Lett.*, 2017, **147**, 2332.

22 M. Elseman, A. E. Shalan, S. Sajid, M. M. Rashad, A. M. Hassan and M. Li, *ACS Appl. Mater. Interfaces*, 2018, **10**, 11699.

23 J. A. Aramburu, P. Garcia-Fernandez, N. R. Mathiesen, J. M. Garcia-Lastra and M. Moreno, *J. Phys. Chem. C*, 2018, **122**, 5071.

24 B. Staskiewicz, O. Czupinski and Z. Czapla, *J. Mol. Struct.*, 2014, **1074**, 723.

25 B. Staskiewicz, I. Turowska-Tyrk, J. Baran, C. Gorecki and Z. Czapla, *J. Phys. Chem. Solids*, 2014, **75**, 1305.

26 Z. Czapla, J. Prezeslawski, M. Crofton, J. Janczak, O. Czupinski and A. Ingram, *Phase Transitions*, 2017, **90**, 637.

27 A. Waskowska, *Z. Kristallogr.*, 1994, **209**, 752.

28 K. Horiuchi, H. Ishihara and H. Terao, *J. Phys.: Condens. Matter*, 2000, **12**, 4799.

29 N. H. Kim, J. H. Choi and A. R. Lim, *Solid State Sci.*, 2014, **38**, 103.

30 A. R. Lim and Y. Paik, *Solid State Sci.*, 2017, **65**, 61.

31 N. Mahfoudh, K. Karoui, M. Gargouri and A. BenRhaiem, *Appl. Organomet. Chem.*, 2020, **34**, e5404.

32 N. Mahfoudh, K. Karoui, F. Jomni and A. BenRhaiem, *Appl. Organomet. Chem.*, 2020, **34**, e5656.

33 N. Mahfoudh, K. Karoui and A. BenRhaiem, *RSC Adv.*, 2021, **11**, 24526.

34 A. R. Lim and S. H. Park, *Molecules*, 2022, **27**, 4546.

35 W. Zang and R.-G. Xiong, *Chem. Rev.*, 2012, **112**, 1163.

36 A. R. Lim and S. H. Kim, *ACS Omega*, 2021, **6**, 27568.

37 R. Kalthoum, M. B. bechir, A. B. Rhaiem and M. Gargouri, *Phys. Status Solidi*, 2021, **218**, 2100485.

38 R. Kalthoum, M. B. Bechir, A. B. Rhaiem and M. H. Dhaou, *Opt. Mater.*, 2022, **125**, 112084.

39 H. Jellali, R. Msalmi, H. Smaoui, S. Elleuch, A. Tozri, T. Roisnel, E. Mosconi, N. A. Althubiti and H. Naili, *Mater. Res. Bull.*, 2022, **151**, 2022.

40 J. L. Koenig, *Spectroscopy of Polymers*, Elsevier, New York, 1999.

41 *SHELXTL v 6.10*, Bruker AXS, Inc., Madison, Wisconsin, USA, 2000.

42 A. R. Lim and J. Cho, *Sci. Rep.*, 2022, **12**, 16901.

43 E. Arunan, G. R. Desiraju, R. A. Klein, J. Sadlej, S. Scheiner, I. Alkorta, D. C. Clary, R. H. Crabtree, J. J. Dannenberg, P. Hobza, H. G. Kjaergaard, A. C. Legon, B. Mennucci and D. J. Nesbitt, *Pure Appl. Chem.*, 2011, **83**, 1637.

44 R. K. Harris, *Nuclear Magnetic Resonance Spectroscopy*, Pitman Pub, UK, 1983.

45 A. Abragam, *The Principles of Nuclear Magnetism*, Oxford University press, 1961.

46 A. R. Lim, *RSC Adv.*, 2021, **11**, 37824.